

# Gravitational wave echoes through new windows

Randy S. Conklin,\* Bob Holdom,<sup>†</sup> and Jing Ren<sup>‡</sup>

*Department of Physics, University of Toronto, Toronto, Ontario, Canada M5S1A7*

There has been a striking realization that physics underlying the black hole information paradox could imply post-merger gravitational wave echoes. We here report on evidence for echoes in the form of tentative signals from four LIGO black hole merger events. For each event, the false-alarm probability is estimated to be less than 1%. Our study begins with the comparison of echoes from a variety of horizonless exotic compact objects. The identification of the more generic features then leads to the development of relatively simple windowing methods, in both time and frequency space, to extract a signal from noise. The time delay between echoes is the primary observable. Our findings from LIGO data point to time delays that are consistent with the deviations from the black hole geometry occurring at the Planck distance from the would-be horizon.

## I. INTRODUCTION

With the discovery of gravitational waves from compact binary mergers [1] came a more careful study of exotic compact objects (ECOs) as alternatives of black holes. Theoretically, the existence of horizonless ECOs may be fundamental to resolving the black hole information paradox. Empirically it is hard to verify the nature of spacetime very close to the horizon due to the large gravitational redshift, and observational evidence from astrophysical objects only shows that ECOs must resemble black holes considerably further from the horizon [2, 3]. Short wavelength modes, which can be approximated by point particles in comparison to the size of the object, have a tiny escape cone and are efficiently trapped in the high redshift region. Very compact ECOs will then appear dark in the electromagnetic window. Gravitational waves with wavelengths comparable to the size of the object may not suffer from the trapping (for a different view involving fuzzballs see [4]).

As recently highlighted in [5, 6], the LIGO observation of the black hole merger and ring-down doesn't exclude horizonless ECOs that have the same light ring potential outside of the horizon. Rather, new observational signals may occur afterwards due to reflection from ECO surfaces or interiors situated well within the light ring. The reflected waves will impinge back on the potential barrier at the light ring after some time delay, with some transmitted to the outside and some reflected back in. This process repeats and generates a distinct set of echoes

---

\* [rconklin@physics.utoronto.ca](mailto:rconklin@physics.utoronto.ca)

† [bob.holdom@utoronto.ca](mailto:bob.holdom@utoronto.ca)

‡ [jren@physics.utoronto.ca](mailto:jren@physics.utoronto.ca)

as seen by an outside observer. The time delay  $t_d$  between two consecutive echoes is closely related to the compactness of the object. Interestingly it depends logarithmically on the distance from the would-be horizon to where deviations occur, and in this way it can probe Planck-scale physics.

A preliminary search for echoes in the LIGO data showed interesting results [7]. That search is based on the traditional matched filtering method with a toy model for the template. Although the significance of the evidence is still under debate [8], this helped to inspire further work on echoes [9–16]. Some of this effort has been put on providing approximate templates for echoes [11, 12, 15].

To move forward, one serious challenge is to deal with the issue of model dependence in the search of echoes. Correlating data with specific templates, which works well for many deterministic signals of general relativity (GR), might not be very efficient for echoes given the variety of ECOs in alternative theories. In this paper we shall explore methods that can extract the main feature of echoes, which is the time delay, while being less sensitive to the more model-dependent information contained in the precise echo waveform. We introduce some of this model dependence as follows.

We start with a static and spherically symmetric background as described by the metric  $ds^2 = -B(r)dt^2 + A(r)dr^2 + r^2d\theta^2 + r^2\sin^2\theta d\phi^2$ . After separating angular variables, the wave perturbation on such a background can be described by a simple field equation

$$(\partial_x^2 - \partial_t^2 - V(x))\Psi(x, t) = S(x, t), \quad (1)$$

where  $x$  is the tortoise coordinate with  $dx/dr = \sqrt{A(r)/B(r)}$  and  $S(x, t)$  denotes the matter source that generates the perturbation. The crucial information about the background space-time is encoded in the effective potential  $V(x) = V(r(x))$ ,

$$V(r) = B(r) \frac{l(l+1)}{r^2} + \frac{1-s^2}{2r} \frac{B(r)}{A(r)} \left( \frac{B'(r)}{B(r)} - \frac{A'(r)}{A(r)} \right), \quad (2)$$

for the field perturbation with spin  $s$  and angular momentum  $l$ .<sup>1</sup> For Schwarzschild black holes,  $V(r)$  describes a potential barrier peaking at  $x_{\text{peak}}$  close to the light ring radius  $r = 3M$ , and it approaches 0 at both spatial infinity ( $x \rightarrow \infty$ ) and the horizon ( $x \rightarrow -\infty$ ).

An ECO with an effective reflecting boundary at some  $x_0 < x_{\text{peak}}$  then behaves as a cavity, with its size (compactness)  $\Delta x = x_{\text{peak}} - x_0$  measured by the time delay  $t_d \sim 2\Delta x$ . The current observation of a clear black hole ringdown phase already requires that  $\Delta x/M \gtrsim 10$  [3]. But more negative  $x_0$ 's remain to be probed, where drastic changes closely related to the fundamental problem of the horizon may occur. For ECOs with deviation only at a proper

---

<sup>1</sup>  $s = 0, 1$  are for the test scalar field, electromagnetic radiation.  $s = 2$  is for the axial metric perturbations in GR. Modified theories of gravity may lead to a different  $V(r)$  for metric perturbations.

Planck distance outside the horizon,  $t_d \lesssim 10^3 M$ , which is of order 0.1s for astrophysical ECOs with  $M$  of order  $10M_\odot$ .

The potentials for ECOs can be quite different at small  $x$ , as shown in Fig. 1. A toy model is provided by a truncated black hole with an interior boundary at some finite  $x_0$ , where the model dependence is encoded in a reflection boundary condition at  $x_0$ . One class of physical models of ECOs is the ultracompact star, for example the gravastar [17, 18], with an exotic matter surface just outside the would-be horizon. The surface location depends on the microscopic physics underlying the exotic matter and no quantitative prediction has yet been made. Such a spacetime is regular and the centrifugal barrier corresponds to a diverging potential at the origin. Recently two of us found another type of ECO, the 2-2-hole [19], with a Planck-scale distance of deviation and a unique interior determined by gravitational field equations. In this case there is no centrifugal repulsion and instead the potential for a test scalar field approaches a finite constant at the origin. The result is a slightly negative deformation small enough to avoid instability. The boundary conditions could also vary significantly for different ECOs. For 2-2-holes a Dirichlet boundary condition automatically emerges at the origin. For ultracompact stars the diverging potential implicitly fixes the boundary condition. Note that we fix  $\Delta x/M = 80$  for all ECOs in both Fig. 1 and later Fig. 2 for illustrative purposes. For a 2-2-hole, the prediction for  $\Delta x/M$  is closer to 400.

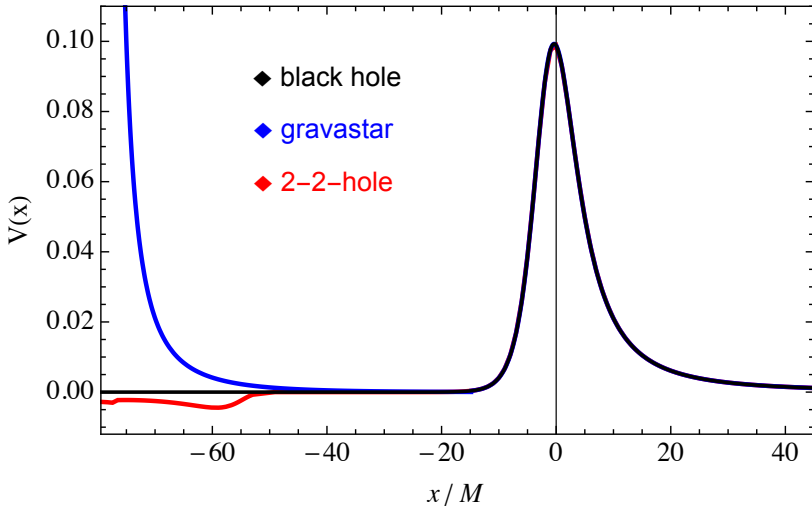


FIG. 1. The effective potential for a test scalar field ( $s = 0, l = 1$ ) on the background of a truncated black hole (black), a gravastar (blue) and a 2-2-hole (red).

In Sec. II we study how the variety of potential shapes and boundary conditions will affect the echo properties, in both the time and frequency domains. We identify properties that are mainly determined by the time delay and that are less sensitive to differences of ECOs. Then in Sec. III we provide search strategies based on windowing methods that can extract the time delay of an echo signal buried in noise. Three methods are developed. In Sec. IV we apply these

search strategies to the LIGO data. Tentative signals are found and false-alarm probabilities are estimated.

## II. GENERAL PROPERTIES OF ECHOES

A useful way to understand echoes is through their frequency content, and detailed analyses along these lines have been carried out in [11, 12]. However those methods cannot be applied to ECOs with potentials significantly different from that of a black hole, like those shown in Fig. 1. So we will first discuss a more general method to find both the universal features of echoes and the non-universal features that can distinguish between ECOs.

Considering a single frequency mode  $e^{-i\omega t}\psi_\omega(x)$  of the field  $\Psi(x, t)$ , the wave equation (1) becomes

$$(\partial_x^2 + \omega^2 - V(x))\psi_\omega(x) = \tilde{S}(x, \omega). \quad (3)$$

$\tilde{S}(x, \omega)$  is the Fourier transform of the source. The solution can be found with the help of the Green's function, which satisfies

$$\frac{\partial^2 G_\omega(x, x')}{\partial x^2} + (\omega^2 - V(x))G_\omega(x, x') = \delta(x - x'). \quad (4)$$

The Green's function can be constructed from the two homogeneous solutions that satisfy boundary conditions on the left ( $x = x_0$ ) and the right ( $x = \infty$ ) respectively,

$$G_\omega(x, x') = \frac{\psi_{\text{left}}(\min(x, x'))\psi_{\text{right}}(\max(x, x'))}{W(\psi_{\text{left}}, \psi_{\text{right}})}. \quad (5)$$

The Wronskian  $W(\psi_{\text{left}}, \psi_{\text{right}}) = \psi_{\text{left}}\psi'_{\text{right}} - \psi'_{\text{left}}\psi_{\text{right}} \equiv W(\omega)$ , which is independent of  $x$  and  $x'$ , contains the essential information of the ECO. Here we assume the outgoing boundary condition  $\psi_{\text{right}} \rightarrow e^{i\omega x}$  when  $x \rightarrow \infty$ . The response to a given source, at spatial infinity  $x \rightarrow \infty$  and at frequency  $\omega$ , is then

$$\psi_\omega = e^{i\omega x} \cdot \mathcal{K}(\omega) \cdot \int_{-\infty}^{\infty} dx' \psi_{\text{left}}(x') \tilde{S}(x', \omega). \quad (6)$$

$\mathcal{K}(\omega) = 1/W(\omega)$  can be viewed as a transfer function fully determined by the properties of the ECO.

For a truncated black hole we consider a one-parameter family of boundary conditions at  $x = x_0$  parametrized by the reflectivity  $R$ ,

$$\psi_{\text{left}} \rightarrow \begin{cases} \frac{1}{2i\omega} e^{-i\omega_V x_0} (e^{-i\omega_V(x-x_0)} + R e^{i\omega_V(x-x_0)}), & x = x_0 \\ A_{\text{out}}(\omega) e^{i\omega x} + A_{\text{in}}(\omega) e^{-i\omega x}, & x \rightarrow \infty \end{cases} \quad (7)$$

where  $\omega_V = \sqrt{\omega^2 - V(x_0)}$ . Once  $\psi_{\text{left}}$  is known then the Wronskian,  $W(\omega) = 2i\omega A_{\text{in}}(\omega)$ , is determined.  $R = 1$  ( $R = -1$ ) corresponds to a Neumann (Dirichlet) boundary condition.  $R = 0$  describes a purely ingoing wave at  $x = x_0$ . The solutions are approximately plane-waves when  $\omega^2 \gg |V(x)|$ . For convenience we choose the normalization of  $\psi_{\text{left}}$  in (7) such that  $\mathcal{K}_R(\omega)$  (labelled by the reflectivity) tends to unity for large  $\omega$  for any  $R$ . This normalization dependence, which also influences the source part, will cancel in  $\psi_\omega(x)$  in (6).

When  $V(x_0)$  is sufficiently small,  $\mathcal{K}_R(\omega)$  is directly related to the transfer function defined in [12]. With the solution  $\psi_{\text{left}}^{R=0}$  that satisfies the purely ingoing boundary condition at  $x = x_0$ , we can rewrite  $\psi_{\text{left}}^R = c_1 \psi_{\text{left}}^{R=0} + c_2 \psi_{\text{right}}$  for any  $R$ . Then  $W_R(\omega) = c_1 W(\psi_{\text{left}}^{R=0}, \psi_{\text{right}}) = c_1 W_{\text{BH}}(\omega)$  and this results in

$$\mathcal{K}_R(\omega) = \frac{1}{W_{\text{BH}}(\omega)} \frac{2i\omega}{(1 - R_{\text{BH}}Re^{-2i\omega x_0})} = \frac{T_{\text{BH}}}{1 - R_{\text{BH}}Re^{-2i\omega x_0}}. \quad (8)$$

$T_{\text{BH}} = 2i\omega/W_{\text{BH}}(\omega)$  and  $R_{\text{BH}}$  are the transmission and reflection amplitudes for the black hole potential. The absolute value of  $\mathcal{K}_0(\omega) = T_{\text{BH}}$  monotonically increases from 0 to 1 as  $\omega$  ranges from 0 to  $\infty$ .  $\mathcal{K}_R(\omega)$  can be calculated even when  $V(x_0)$  is non-negligible. With ingoing/outgoing waves at  $x = x_0$  defined in terms of the modified frequency  $\omega_V$ , (8) can be viewed as a generalization of the definition in [12] with modified transmission and reflection amplitudes.

Our definition of the transfer function  $\mathcal{K}(\omega)$  can be applied to other ECOs with arbitrary potentials and boundary conditions. Fig. 2 shows how a variety of ECOs influences the transfer function. Fig. 2(a) shows the truncated black hole for the  $s = l = 2$  axial metric perturbation and with various boundary conditions. Fig. 2(b) shows the generalized transfer functions for a 2-2-hole and two types of gravastars. The main observation from these figures is that the different ECOs produce resonance patterns that differ mostly by an overall shift, except at the lowest frequencies where nontrivial distortions occur. And away from the lowest frequencies, the peaks are close to being evenly spaced.

In Fig. 2(a) we have chosen to plot  $|\mathcal{K}_R(\omega) - \mathcal{K}_0(\omega)|$ , where the subtraction corresponds to subtracting away the high frequency component. The result involves at least one factor of the reflection amplitude, and the smooth decrease seen at high frequency confirms that no pure transmission term remains. For the 2-2-hole the metric perturbations are described by the more complicated equations from quadratic gravity, but for illustrative purposes we have carried over to the  $s = 2$  effective potential the small  $r$  deformation occurring for the scalar field. We see that the effect of such a deformation away from the truncated black hole with  $R = -1$  is quite mild except at very small frequencies. For the gravastar we impose the boundary condition slightly off the center with the series expansion,  $\psi_{\text{left}} = a(x - x_0)^{l+1}$ . The coefficient  $a$  is chosen such that  $|\mathcal{K}(\omega)| \rightarrow 1$  at high frequencies. The two choices of the gravastar parameters give a large relative shift in the resonance pattern.

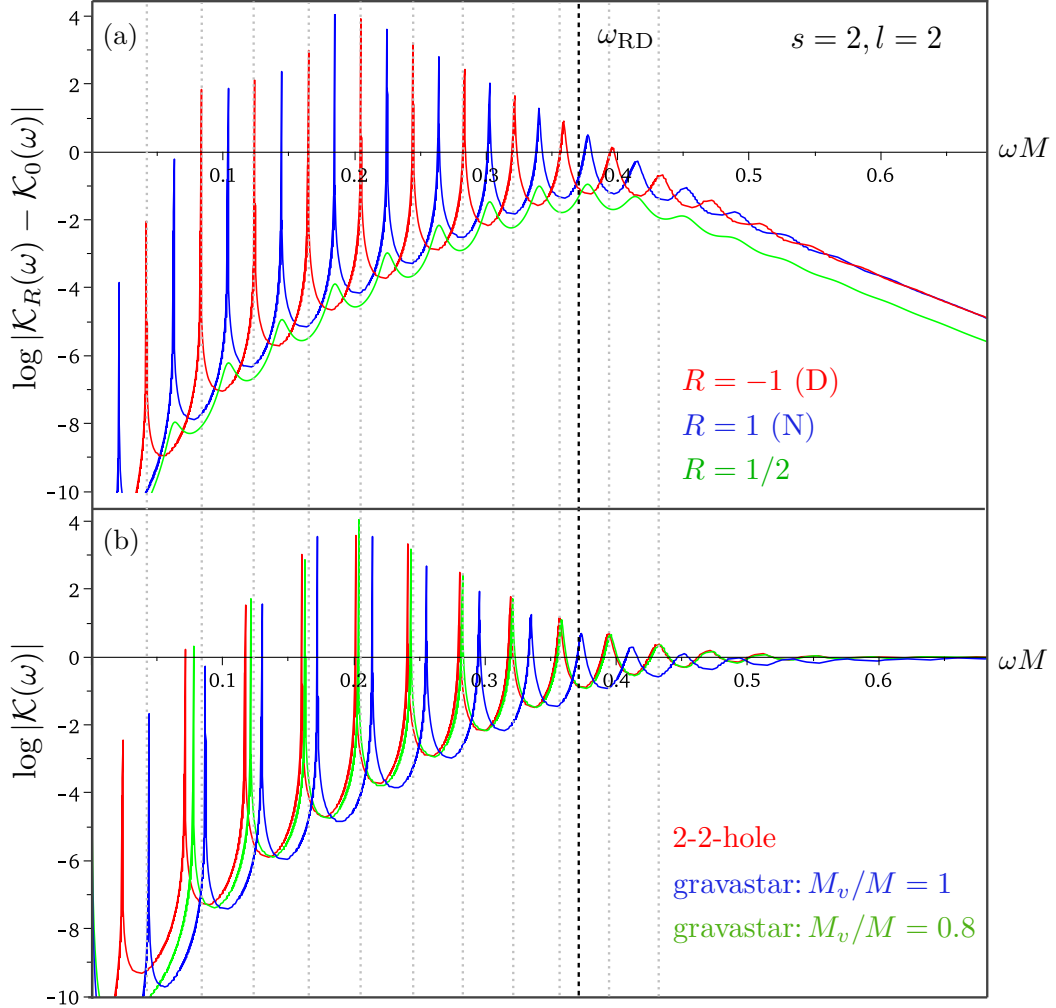


FIG. 2. Upper:  $\log(|\mathcal{K}_R(\omega) - \mathcal{K}_0(\omega)|)$  for the truncated black hole:  $R = -1$  (red),  $R = 1$  (blue),  $R = 1/2$  (green). Lower:  $\log|\mathcal{K}(\omega)|$  for 2-2-hole (red), gravastar with  $M_v/M = 0.8$  (green), gravastar with  $M_v/M = 1$  (blue). All assume  $\Delta x/M = 80$ .  $\omega_{\text{RD}}$  denotes the black hole ringdown frequency.

The resonance spikes for real frequencies correspond to complex poles of the Green's function that are close to the real axis. The real part of the resonance positions  $\omega_{iR}$  vary depending on the boundary conditions and shape of the potential. The spacing between two consecutive resonances is typically  $2\pi/t_d$  with deviations occurring for the low frequency modes. The resonance widths become narrower for smaller  $\omega_{iR}$ , corresponding to the drastically decreasing imaginary part. For resonances below the black hole ringdown frequency  $\omega_{\text{RD}}$ , the WKB approximation gives  $|\omega_{iR}| \approx e^{-\Gamma}/2t_d$ , where  $e^{-\Gamma}$  is the tunneling rate associated with the black hole potential for a given  $\omega_{iR}$  [20].

The echo waveform in the time domain can be found through an inverse Fourier transform. But it is more instructive to obtain it by solving the wave equation (1) numerically, with the appropriate boundary condition at  $x = x_0$ . The source dependence is replaced by using a Gaussian pulse as an initial condition, where its width determines the range of frequencies

being considered. The initial Gaussian that starts inside the light ring can model an outgoing perturbation from the interior, which could be appropriate for conditions just after the merger of comparable-mass compact binaries. The initial Gaussian traveling towards the light ring from the outside is better suited to model a merger in the extreme mass ratio limit. In the former case the first pulse corresponds to transmission, while in the latter case it is a reflection. Since the light ring potential serves as a high-pass filter for transmission and a low pass filter for reflection, in the former and latter cases the first and second pulses contain high frequency components respectively. In either case we identify the first pulse with the ringdown phase of the merger event and the subsequent pulses as the echoes.

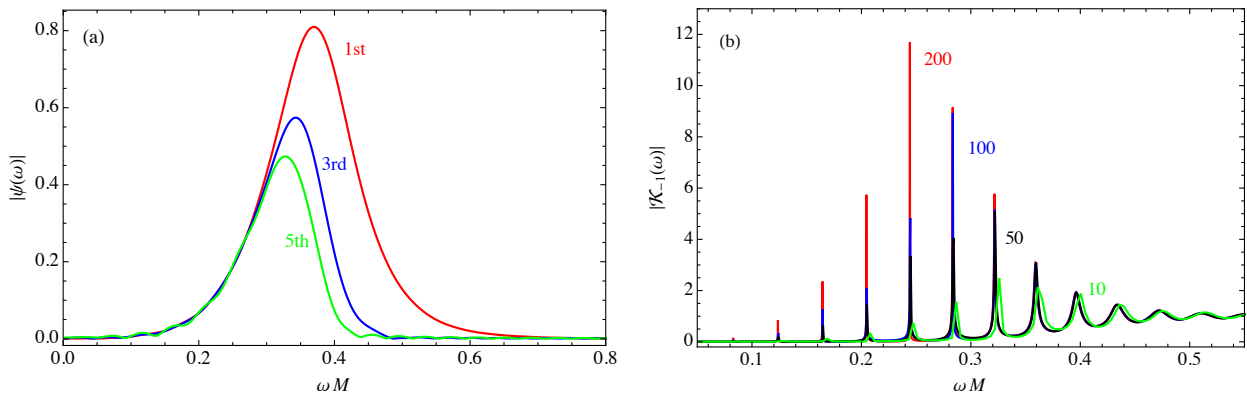


FIG. 3. For a truncated black hole with  $R = -1$ ,  $\Delta x/M = 80$  and the initial Gaussian pulse within the light ring: (a) the frequency content of various echoes; (b) the reconstructed transfer function with different echo numbers.

Fig. 3(a) presents the frequency content of various echoes as generated by an outgoing initial Gaussian pulse within the light ring for a truncated black hole. Since the later echoes involve transmission and more reflections, the result is a frequency content slowly shifting downwards. In the time domain this corresponds to gradually growing widths of echoes, which can eventually overlap at late enough times. We find that the echo widths and their growth are relatively universal for various ECOs, meaning that this is largely determined by the shape of the potential barrier. In particular the width is  $\sim 100M$  for the first echo,  $\sim 320M$  for the 19th echo and it grows at a constant rate of  $\sim 12M$ . The potentials that we have investigated that differ at small  $x$  can lead to small deviations from this universal behaviour. This occurs mainly for the later echoes that are dominated by lower frequencies.

The transfer function  $\mathcal{K}(\omega)$  can be reconstructed by the Fourier transform of echoes normalized with the frequency content of the initial Gaussian. The contribution from the first pulse is simply the transmission amplitude, i.e.  $\mathcal{K}_0(\omega)$ , and the subsequent echoes correspond to  $\mathcal{K}_-(\omega) - \mathcal{K}_0(\omega)$ . Fig. 3(b) shows the reconstructed  $|\mathcal{K}_-(\omega)|$  with different frequency resolutions. With an increasing number of echoes, more points contributing to the resonance spikes are sampled, and the resonances at lower frequency with narrower widths are gradually re-

covered. As another example, resolving all resonances down to  $\omega M \sim 0.3, 0.25, 0.2$  requires the number of echoes  $N_E \sim 60, 400, 4000$  respectively. In practice, a set of lower resonances that are only partially sampled can still usefully contribute to a signal.

For the LIGO merger events, the final objects have spins and the observations already require them to resemble the exterior Kerr black holes at least down to the light ring radius. We can expect that the generic features of echoes will remain similar for rotating ECOs. Although the boundary conditions or the shape of potentials at small  $x$  in the perturbation equation could change, the resonance pattern should continue to stretch up to roughly the ringdown frequency of the Kerr black hole. This is because the growing width and decreasing height of the resonance peaks is controlled by the tunnelling through the potential barrier at the light ring. But the rotation causes the shape of the potential barrier to change, and so this can change the shape of the resonance pattern.

In summary, for different types of ECOs, the absolute value of the Fourier transform of the echo waveform is universally characterized by nearly evenly spaced resonances with gradually increasing widths. As a generic search target, we look for this resonance pattern within a frequency range centered somewhat below the ringdown frequency of the corresponding black hole. The reasons for a restricted frequency range are fourfold. 1) For the transfer function we see that the heights of resonances grow at lower frequency and reach a peak at some intermediate value for a given frequency resolution. 2) By cutting off the lowest frequencies, we remove most of the model-dependent deviation from constant resonance spacing. 3) Restricting the frequency range reduces the dependence on the low and high frequency content of the initial condition (or source), which may not be well known. 4) The frequency range we aim for will be within the optimal band for the gravitational wave detectors whenever the black hole ringdown frequencies are also in this range.

### III. SEARCH STRATEGIES FOR ECHOES BURIED IN NOISE

We now want to make use of the generic features of echoes to help extract them from noise. Here we propose to use window functions in the time and/or the frequency domains to reduce noise. The windows are mainly defined by the time delay, and together with some other parameters that encode the generic features of echoes, their construction is much simpler than modelling the waveform with a template. We shall also rely on the expected correlation of a signal in multiple gravitational wave detectors to further reduce the noise. By using different windows, we describe three methods to find correlations between data sets with respect to different quantities. A final correlation with respect to the time delay is used to identify the signal. In this section the methods are tested by toy models with a sample signal combined with two different sets of Gaussian noise, to model the real data from the two LIGO detectors. The range of window parameters that work in the toy model then serves as the basis for the

real data search in Sec. IV. It should be noted though that the toy model was investigated for time delays that were of interest for the real data search; for very different time delays the window parameters we choose here might not be appropriate.

### A. Windows in the time domain

Very compact ECOs have a large time delay and thus have many distinct echoes after ring-down. One strategy for removing noise is to impose a time window function that, when multiplied onto the data, zeros the data between echoes. Such a window function is primarily described by the following parameters: the time delay  $\Delta t$  between centers of windows, the time at the center of the first window  $t_0$ , the window width  $t_{wi}$  for the  $i$ th window, and the total time duration  $T$  of the data to be windowed. As a reference time we choose  $t_{\text{merger}}$ , a time that is accurately determined from the main event. Then we allow the time of the first window to shift within the range  $t_{\text{merger}} + 0.9\Delta t < t_0 < t_{\text{merger}} + 1.1\Delta t$ . Since the typical  $\Delta t$ 's of interest are much larger than the duration of the merger, this range should be more than enough to account for any effect the merger dynamics can have on  $t_0$ .

The simplest choice is a square window of unit height and constant width  $t_w$ , but this ignores the shape and growing width of the echoes as described in the previous section. To improve on square windows for this method we first smooth the edges by using Hann windows. These are given by  $\frac{1}{2}(1 + \cos(2\pi x))$  for  $-\frac{1}{2} \leq x \leq \frac{1}{2}$  and 0 elsewhere. To account for the steadily increasing widths of echoes we use windows with  $t_{wi}/M \sim 100 + 12i$ . Since the early echoes are more asymmetric, we shift the earlier windows slightly earlier so that the peaks of the windows line up better with the peaks of the echoes. Fig. 4 presents an example of the improved window function.

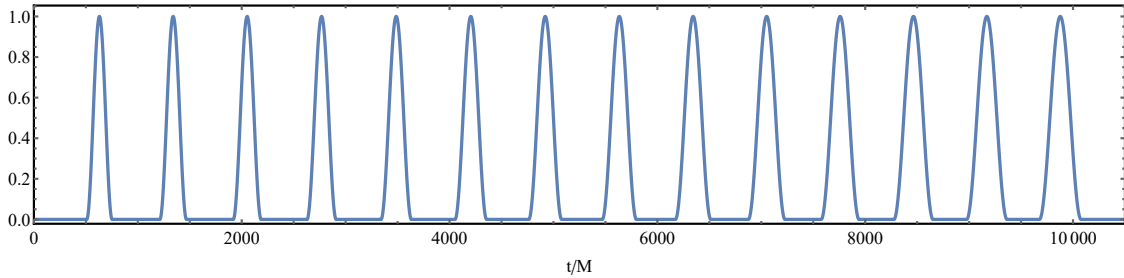


FIG. 4. Fourteen Hann windows with increasing widths and  $\Delta t/M = 780$ .

We next have to decide on the number of windows to include. This is determined by a tradeoff between the signal resolution and noise reduction. The frequency resonance structure can be better reconstructed by including more echoes, that is a larger  $N_E = T/t_d$ . On the other hand the later echoes become smaller in amplitude and wider in width. Thus the gain in the signal-to-noise ratio (SNR) for increasing  $N_E$  eventually stops, typically when the echoes start

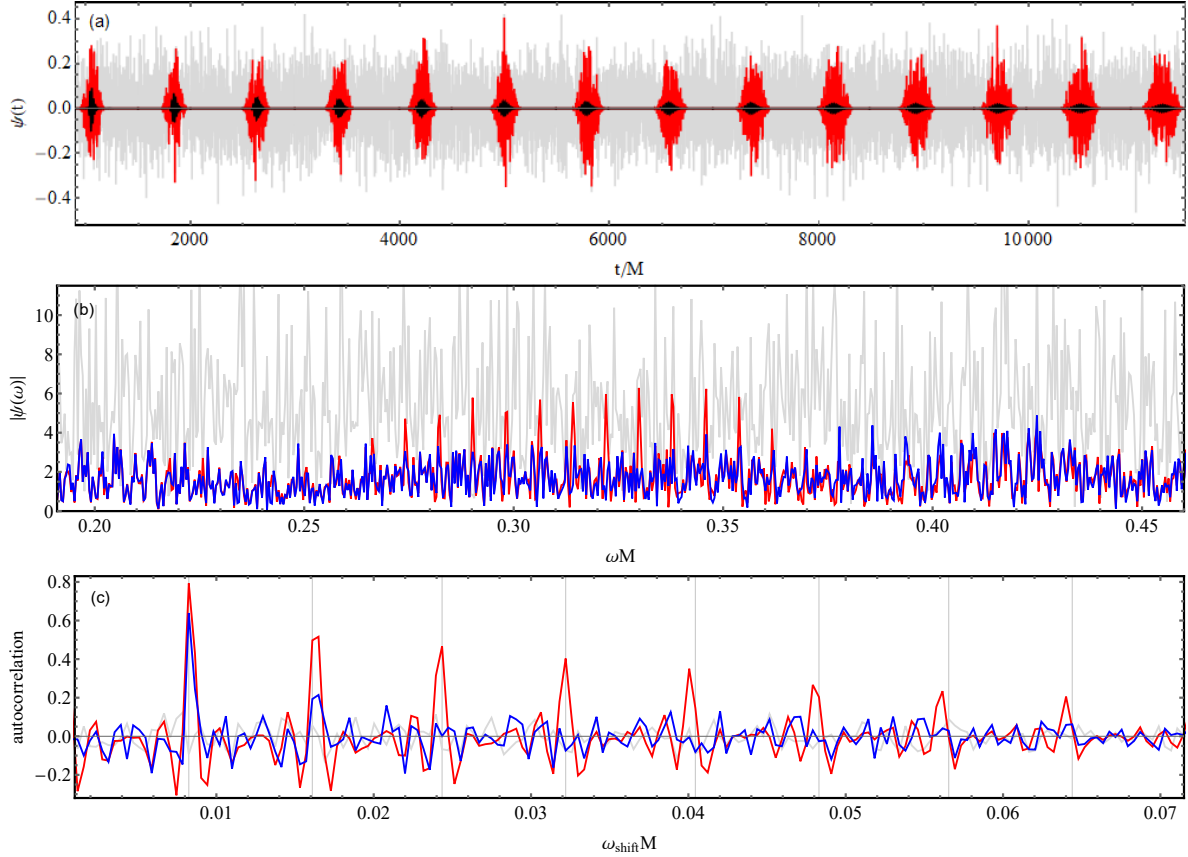


FIG. 5. (a) Echoes combined with Gaussian noise in the time domain. (b) The absolute value of the Fourier transform of the data. (c) Autocorrelation function of the data in (b) with  $\omega \in (0.7, 1)\omega_{\text{RD}}$ . The black shows the signal, the grey and red show the data before and after windowing and the blue shows the windowed Gaussian noise.

to overlap. From the toy model it was found that  $N_E \sim 15-50$ , with an even smaller range being optimal for increasing noise.

Fig. 5(a) shows the windowed data set, where the window aligns with the sample signal. We then proceed to Fourier transform the windowed data and take the absolute value to search for the resonance structure in frequency space. The impact of the time window is illustrated in Fig. 5(b). The signal resonance pattern emerges after windowing (red curve), in comparison to the noisy distribution before windowing (gray curve) and the windowed version of the pure noise (blue curve). The latter shows that the window also generates artifacts that can mimic a signal, i.e. equally spaced spikes due to the periodicity of the window itself. However the artifacts are more spread out in location and random in size compared to the signal peaks. This allows us to apply a bandpass  $f_{\min} < f < f_{\max}$ , and the toy model suggests that a reasonable bandpass is  $(f_{\min}, f_{\max}) \sim (0.7, 1)f_{\text{RD}}$ , where  $f_{\text{RD}}$  is the corresponding black hole ringdown frequency.

The signal resonances in Fig. 5(b) can be further isolated by forming the autocorrelation

function of the Fourier transformed data within the selected bandpass. As shown in Fig. 5(c), where the autocorrelation is plotted as a function of shift, a series of peaks will occur for shifts coinciding with the resonance spacing (vertical grey lines). The noise due to the windowing artifacts enters into the first two peaks (blue curve). So for a given window and frequency bandpass, we sum over a subset of the later peaks to produce a single amplitude. For the time delay used in the figure, a good subset to use is peaks 3 to 8.<sup>2</sup>

Thus for a data set  $i$  and a time delay  $\Delta t$ , we have an amplitude  $A_i(s)$  as a function of the offset  $t_0 = t_{\text{merger}} + 0.9\Delta t + s\delta t$ , for integer  $s$  and increment  $\delta t$ . In the presence of a common signal in two data sets then  $A_1(s)$  and  $A_2(s)$  will become large at the same  $s$  and if  $\Delta t$  is the actual time delay. Thus we consider the maximum of the following products,<sup>3</sup>

$$\text{Max}(\{A_1(s)A_2(s), s = 0, \dots, 0.2\Delta t/\delta t\}). \quad (9)$$

The signal now appears as a peak in this correlation when considered as a function of  $\Delta t$ . This gives our estimate for the actual time delay  $t_d$ , and the optimal offset  $t_0$  is also determined.

## B. Windows in the frequency domain

Another strategy is to directly Fourier transform the time series data of some duration  $T$  and then impose a quasi-periodic window in frequency space to remove noise between the resonance spikes. It is then not necessary to precisely line up the time series of the two detectors. The frequency window function is characterized by a similar set of parameters: the window spacing  $\Delta f$ , the offset  $f_0$ , the widths  $\{f_{wi}\}$ , and the bandpass  $f_{\min} < f < f_{\max}$ . This method does not rely on having clearly separated echoes in the waveform. Including overlapping echoes at late time with larger  $T$  increases the frequency space resolution, and can help to resolve lower frequency resonance spikes with very narrow widths. But again there is a trade-off that determines an optimal range for  $T$ .

The simplest window is of a square shape with unit height and constant width. But we find it advantageous to move to a window of trapezoidal shape, being purely triangular for low frequencies where the spikes are sharp, to a gradually wider shape at higher frequencies where the resonance peaks are wider and lower. We illustrate this window function in Fig. 6. The basic frequency increment is  $1/T$  and the triangular window (the narrowest of the windows) is nonzero over 11 such increments. From the results of the toy model we choose to adopt this as a universal window construction for this method, where the window widths are defined once and for all, for all analyses.

---

<sup>2</sup> Generally the windowing artifacts are larger the narrower the window width is compared to the time delay. The time delays at the high end of the range we consider in the LIGO search will prompt us to use peaks 5 to 8.

<sup>3</sup> A more sophisticated version of this correlation could be tried as in (11) below, but the toy model does not show a strong preference for this here.

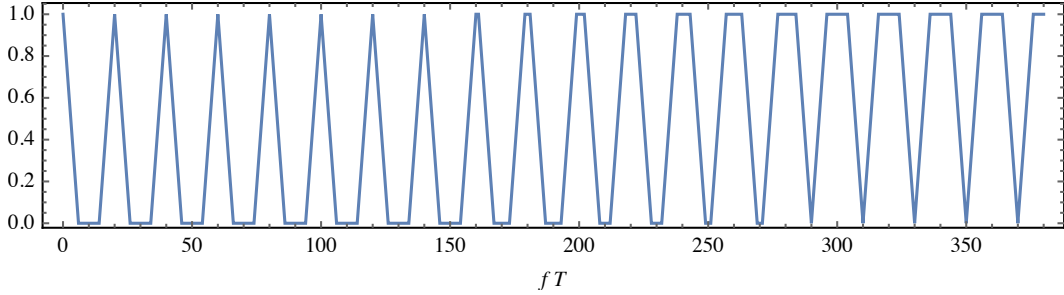


FIG. 6. An example frequency window function with a spacing  $T\Delta f = 20$ . A more typical window for the real data analysis would have the same range of widths but with  $T\Delta f = 200$  and about 50 windows within the bandpass.

We take the absolute value of the Fourier transform of some dataset  $i$  of duration  $T$ . Let  $S_i(n_m, n_M)$  be the segment of the resulting series within the bandpass  $(f_{\min}, f_{\max}) = (n_m, n_M)/T$ . Let  $W(n, s)$  denote the window function where the integer  $n = T\Delta f$  is the window spacing in units of the basic frequency increment, and  $s = \{1, 2, \dots, n\}$  is the offset.  $W(n, s)$  is a vector having the same length as the data set  $S_i(n_m, n_M)$ . For a given  $n_m$ ,  $n_M$  and  $n$  we then construct an amplitude as a function of the offset,

$$A_i(s) = \text{Mean}(S_i(n_m, n_M) * W(n, s)). \quad (10)$$

Here the Mean is taken on the nonzero products of the components of the two vectors.

For a signal,  $A_i(s)$  will have larger values over a range of  $s$  that is roughly twice the window width. Thus we form another vector with 22 1's and  $(n - 22)$  0's. Let  $V_r(s)$  be this vector after performing a cyclic rotation of the elements  $r$  times. Now we can construct the following correlation between the two data sets,

$$\text{Max}(\{\text{Corr}(A_1, V_r)\text{Corr}(A_2, V_r), r = 1..n\}), \quad (11)$$

where Corr is the standard Pearson correlation. The maximum of the products of the correlations will be large if a repeating resonance structure in frequency space is lining up (has the same offset) in the two detectors. This final correlation between detectors is still a function of  $n$ , and a signal appears as a peak as  $n$  is varied. The location of the peak defines a particular  $n_d$  that gives an estimate of the actual time delay  $t_d$  as  $n_d = T/t_d = N_E$ . The range of  $n$  translates to a range of time delays that are being tested. From the preferred value of  $r$  in (11), the optimal offset  $s$  (or  $f_0$ ) of the window function is determined. This could then be used to distinguish ECOs with different potentials and boundary conditions, as shown in Fig. 2.

From the toy model we find that the bandpass  $(f_{\min}, f_{\max}) = (1/4, 5/4)f_{\text{RD}}$  is a reasonable choice for this method. For the time delays of interest for our search  $f_{\text{RD}} \sim 50/t_d$ . We also find that the best SNR for this method occurs for echo numbers  $N_E \approx 100\text{-}300$ . The persistence

of a signal peak for a range of  $N_E$  helps to differentiate it from a noise peak, which typically shows less persistence. We thus find that it is effective to average the final correlation plots for a range of  $N_E$  to enhance the SNR.

### C. Combining time and frequency windows

The two methods with windows in time or frequency space are complementary to each other. The separation between the echoes in the time domain and the separation between the resonances in the frequency domain are inversely related to each other. So for long (short) time delay the time (frequency) windows are more effective at removing noise. But it is still possible that applying both time and frequency windows could remove even more noise. This hybrid approach might be expected to work best for intermediate time delays.

As an illustration of the hybrid approach, our method III uses simplified square windows with constant width in both the time and frequency domains. These windows are characterized by the parameters  $\Delta t$  ( $\Delta f = 1/\Delta t$ ),  $t_w$ ,  $T$ ,  $f_0$ ,  $f_w$ ,  $f_{\min}$  and  $f_{\max}$ . We choose to restrict the time window offset  $t_0$  to be around the expected value,  $t_0 \approx t_{\text{merger}} + \Delta t$ . Since echoes grow wider at later times, there is a trade-off in choosing  $t_w$  to capture the dominant content of echoes with the minimum amount of noise. In particular a too small  $t_w$  will spread out the signal resonance pattern and make it less distinctive from noise.

For a given set  $\{t_w, T, f_w\}$  we take the mean of the absolute value of the doubly windowed data  $A_i(s)$  defined analogously to (10). Then we find the frequency window offset  $s$  that maximizes the correlation between two data sets,  $\text{Max}(\{A_i(s)A_j(s), s = 1..n\})$ . Finally the bandpass  $f_{\min} < f < f_{\max}$  is optimized to find a peak in these maximum correlations as a function of  $\Delta t$ . In this hybrid method different window parameters are more correlated, making it more difficult to identify their optimal values. It could be expected that the time window artifacts make the frequency window less effective. But the advantage of the frequency window is that it brings in the use of the correlation with respect to the offset  $s$ .

From the toy model study, we find that this method starts to work with relatively small echo numbers, i.e.  $N_E = 10\text{-}20$ . The optimal time window width, which is around  $t_w/M = 40\text{-}80$ , is narrower than the real echo widths. For these relatively small choices for  $T$ , the frequency space resolution is low, and we need the small values  $f_w T = 1\text{-}3$  to best capture the signal. With different choices of  $\{t_w, T, f_w\}$ , signal peaks are found to persist more than noise peaks. Thus we average over them all to increase the SNR, after we shift and normalize each correlation plot to have zero mean and a common variance. Higher values of  $N_E$  could also be expected to work, but they are not considered in this paper.

#### IV. EXPLORATION OF THE LIGO DATA

We now apply the search strategies described in Sec. III to the LIGO data. We use the strain data of the two LIGO detectors for the five confirmed events of binary black hole coalescence[1, 22–25] provided by the LIGO Open Science Center [21]. Our methods need some signal strength in both detectors, but otherwise they are not sensitive to relative phases between detectors due to different projections of the polarization. The latter effect is in any case minimized for the two LIGO detectors due to their similar orientation.

For the signal search we apply the three window methods to the whitened data after merger. We find evidence for echoes that is accumulating in the form of a number of tentative signals. Method II finds signals for GW170104, GW170608, GW151226 and GW170814 in decreasing order of strength. Method I finds a signal for GW151226, where the best-fit  $t_d$  matches that of method II very closely. Method III finds a signal for GW170814, and the agreement with method II on  $t_d$  is also good. Since methods I and III explore data of much shorter duration than method II, the agreement of the tentative signals for these two events serves as a nontrivial consistency check. Of the five events we have considered, none of our methods have yet found a significant signal for GW150914. This event is both the earliest and the loudest, but the noise characteristics of the two detectors relevant for our search may be improving over time.

We searched for signals over a wide range of time delays that includes what one might expect for a deviation occurring at a proper Planck length from the would-be horizon. Our signal plots and our background analysis plots for the four events are collected in the four figures Figs. 7–10. On each signal plot the red curve denotes the final correlations between two detectors as a function of the time delay. For comparison the blue curve in each plot shows the result of applying the same procedures to data of the same duration occurring just before merger. Each plot shows the range of time delays covering  $\pm 30\%$  from the central peak, and each curve is adjusted to have zero mean.

To assess the significance of each signal peak we find the false-alarm probability, which we simply refer to as a p-value. We follow our same procedure for the same time delay range on some number of trials, based on various time-translated parts of the LIGO data. The black curve shows the probability of finding a highest peak of equal or greater height compared to the midpoint bin value. This is determined from the listed number of trials. The red dot denotes where the signal peak is, from which we can find the p-value. Method I and method III only require a short range of data and so with the full one hour of LIGO data we can generate a sufficient number of independent background trials in this way. Method II uses larger echo numbers and thus a longer range of data is needed for each background trial. To generate a sufficient number in this case we employ varying time shifts between pairs of segments from the two detectors. (For GW170608 we use only 512 seconds of noise-subtracted data, which is all that is available.)

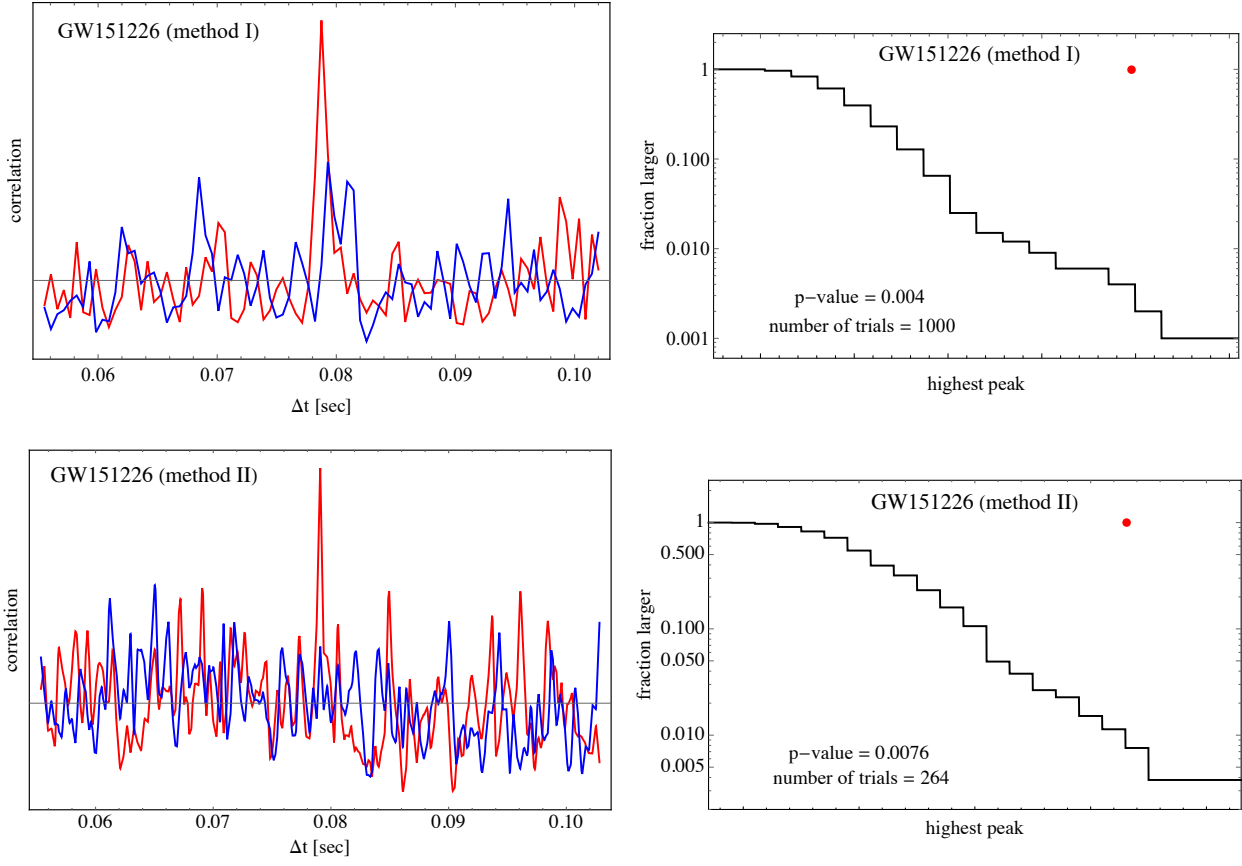


FIG. 7. Event GW151226, methods I and II. The final correlation of two of the LIGO detectors as a function of the time delay, for the signal search (red) and one background search (blue). On the right, p-values from the number of background trials given.

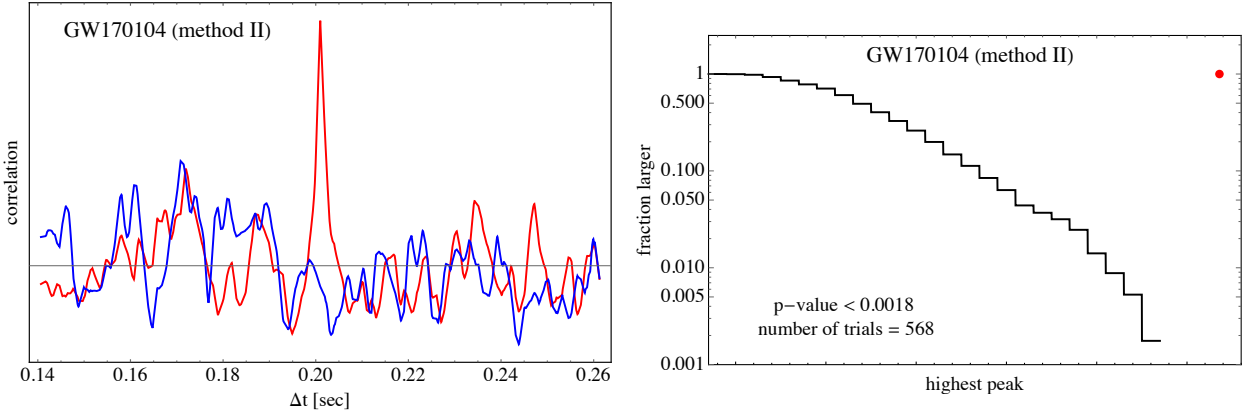


FIG. 8. Event GW170104, method II.

From the reported uncertainties in the final object's mass, we find that the tentative signals for the four events have values of  $t_d/M$  that are consistent with each other and with the predicted range  $700 \lesssim t_d/M \lesssim 860$  for a spinless 2-2-hole [19] (what spin does to this result is unknown). Our values of  $t_d$  are a little smaller than those considered in [7]. Our p-values are

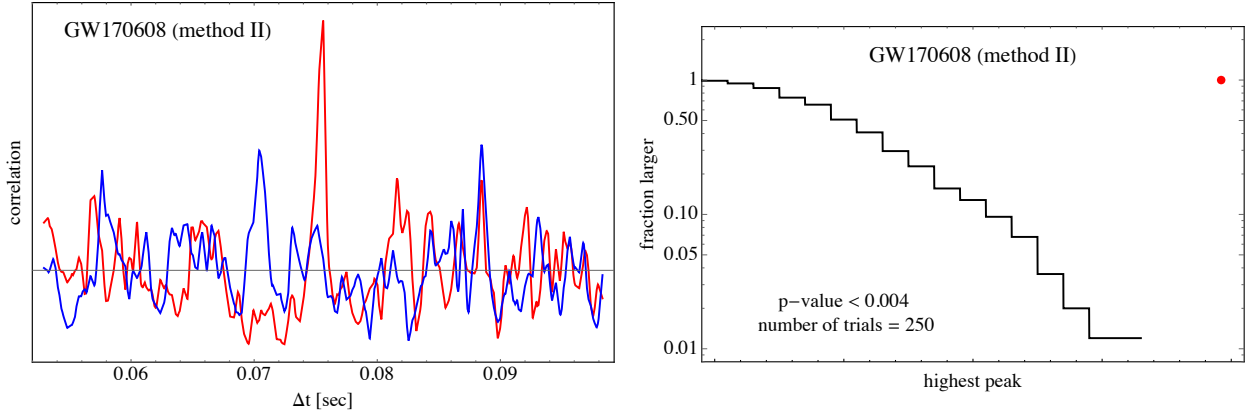


FIG. 9. Event GW170608, method II.

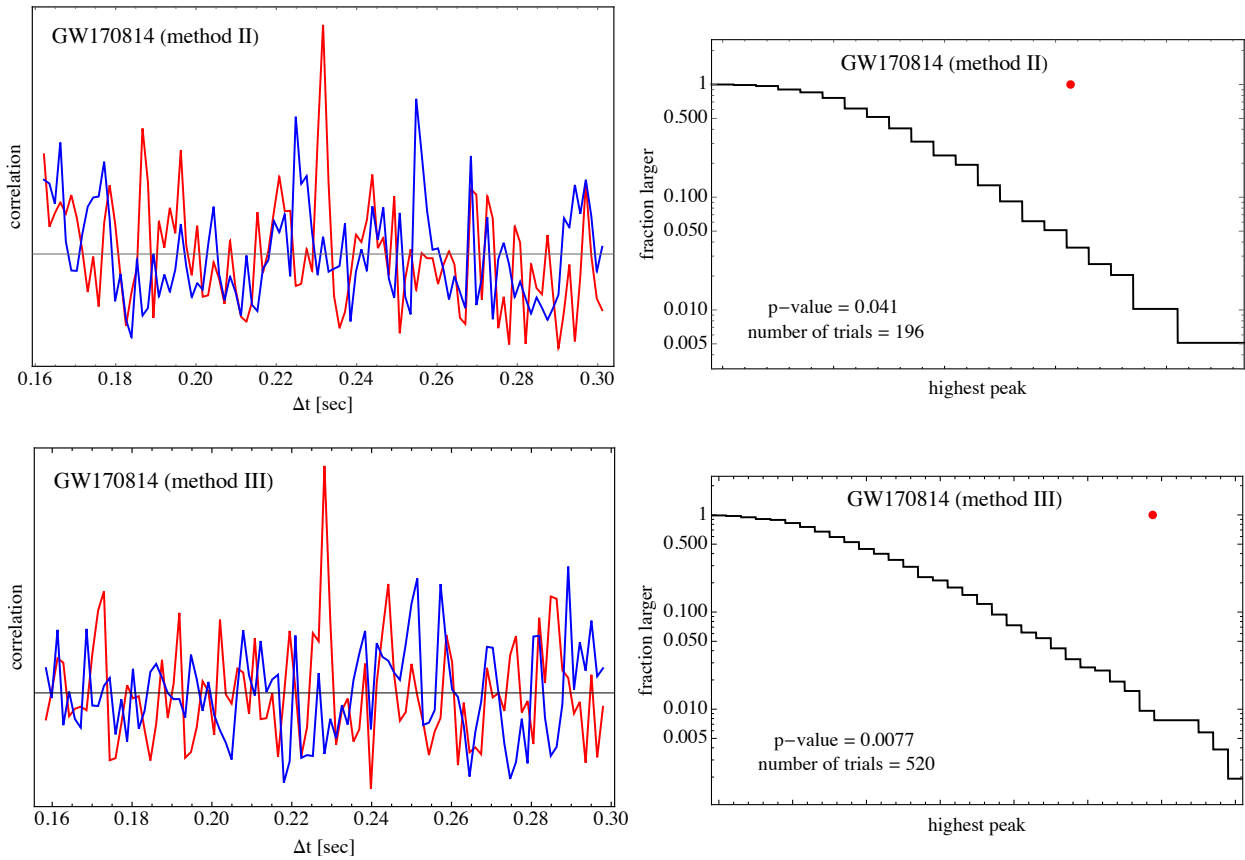


FIG. 10. Event GW170814, methods II and III.

essentially proportional to the time delay range tested, in our case  $\pm 30\%$  around the central peak. Given that the time delay has a log dependence on a distance from the would-be horizon, this range corresponds to exploring length scales with a  $\mathcal{O}(10^{20})$  range around the Planck distance. This range is significantly wider than that used in the template search [7]. For GW151226, the only event where we both observe signals, their range does not include our value for  $t_d$  while our range does include their's.

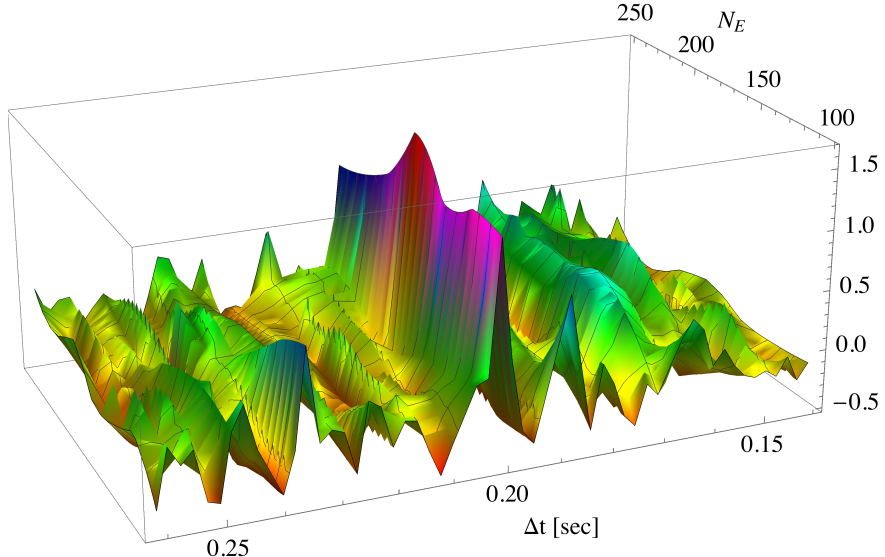


FIG. 11. Correlation vs. time delay for different  $N_E$  for GW170104 with method II.

TABLE I. The best-fit  $t_d$ , bandpass and window parameters used for the six tentative signals.

Event (method)	Best-fit $t_d$ (sec)	Bandpass ( $f_{\min}, f_{\max}$ ) $t_d$	Window parameters used for average (other parameters defined in Sec. III)
GW151226 (I)	0.0788	(30, 64)	$N_E = (1-29), (5-29), (9-29)^*$ (*echoes 9 through 29 were used)
GW151226 (II)	0.0791	(12, 58)	$N_E = (260, 270)$
GW170104 (II)	0.201	(16, 62)	$N_E = (100, 125, 150, 175, 200)$
GW170608 (II)	0.0756	(14, 60)	$N_E = (140, 200, 260)$
GW170814 (II)	0.232	(12, 58)	$N_E = (170, 170^*)$ (*the whole time range used was shifted 10 seconds later)
GW170814 (III)	0.228	(30, 70)	$(N_E, t_w/M) = (15, 40), (10, 80), (15, 80), (3-15, 40), (5-17, 40), (3-15, 80)$

A signal peak tends to persist over various changes of the window parameters more so than a noise peak. Fig. 11 shows an example of the persistence of the signal peak as a function of  $N_E$  for GW170104, which makes clear that an averaging of the correlations over  $N_E$  will improve the signal.<sup>4</sup> Thus we have used an averaging over  $N_E$  and sometimes other window

<sup>4</sup> With spin the late time echoes might then have increasing amplitudes due to the superradiance amplification of the low frequency modes [3, 26]. A rough estimate implies that this could occur after 100-200 echoes, which

parameters to produce the final signal plots.

This is summarized in Table I along with the best-fit values of  $t_d$  and the frequency bandpass used in each analysis. We express the bandpass as a dimensionless range,  $(f_{\min}, f_{\max})t_d$ , where we use  $t_d$  since it is being determined to greater accuracy than  $M$  or  $1/f_{\text{RD}}$ . In method II the bandpass stays quite stable over the four events as it varies between  $46 \times (.25, 1.25)$  to  $46 \times (.35, 1.35)$ , while for the other two methods it shifts higher. This suggests that the low frequency narrow spikes play a more significant role in method II as might be expected. Table I also shows several instances where leaving out some number of the early echoes can positively contribute to the strength of the signal.

Values of  $t_d$  are determined from two different methods for GW151226 and GW170814, and the agreement is within 0.5% and 2% respectively. Such differences could be expected since  $\Delta t$  in our different methods aims to capture the leading order constant spacing between echoes or frequency resonances. Deviations from the constant spacing, which depends on the model of ECOs, can then influence the best-fit  $t_d$  in different methods at the percent level.

Methods I and III are able to determine the optimal  $t_0$  (the time of the first echo) at the best-fit time delay  $t_d$ . We find  $t_0 - t_{\text{merger}} = 0.941t_d$  and  $t_0 - t_{\text{merger}} = 0.984t_d$  for GW151226 and GW170814 respectively, where there are probably modelling uncertainties of a few percent. Method III also finds that the optimal values of the frequency window offset  $f_0$  are consistent for different windows.

As a further check on an echo interpretation of a peak showing up at a certain time delay  $t_d$ , weaker peaks could also be expected at exactly  $t_d/2$  and  $2t_d$ . In these cases the window function would be either under-sampling or over-sampling the actual periodic spikes in the data. A peak faked by random noise is less likely to have the corresponding secondary peaks. With method II we see evidence of both types of secondary peaks for GW151226 and GW170608, and for GW170104 the secondary peak at  $t_d/2$  is quite prominent.

We also check the influence of the whitening process on our tentative signals. The power spectral density that is used in the whitening is obtained by averaging over some number of time segments, whose length determines the resolution for the whitening. Shorter segments tend to leave more detector artifact spikes in the whitened data. But longer segments modify the raw data on finer frequency scales, and so there is risk of modifying the sharp spikes of the signal. This seems to be the case for method II where the signal is diminished for longer time segments. For method II we use 1s segments, and we find that the results change little whether or not we manually remove the resulting obvious noise spikes. For method I (III) the signal peak remains similar for either 1s or 3s (4s) segments, and a 1s (4s) segment is used.

Our initial p-value estimation overlooks some additional sources of look-elsewhere effects due to window parameters that are fixed by their signal search values and possible priors on

---

is similar to the range of  $N_E$  in Fig. 11. But the  $N_E$  dependence seems consistent with the toy model that has no superradiance.

these parameters. One example is the frequency bandpass that is fixed by the signal search. In method II we learn from the toy model that there is a rough prior  $N_E \sim 100\text{-}300$  that peaks somewhere in the middle of this range. For GW170104 and GW170608 a sizable portion of the 100-300 range is used. For GW151226 and GW170814 only a small part is used, thus implying a larger look-elsewhere effect. Similarly for method I some particular ranges of  $N_E$  are used which in this case indicates that the later echoes are relatively important for the signal. For method III, so far only small values of  $N_E$  have been tested, and values of  $(t_w, f_w)$  used are expected to be quite typical, but a choice of particular combinations of  $t_w$  and  $N_E$  is made. And finally, the position of the signal peaks are determined to greater accuracy than the discreteness so far described in the method definitions. This is possible because the signal peaks are sharp relative to the discreteness and they can be resolved at higher resolution. But we have not determined as precisely the position of high peaks in the background trials.

From this discussion we see that further studies on both toy models and background analysis could help to improve the p-value estimates. It will be helpful to better understand the behaviour of the proposed test statistics and to refine the prior of various window parameters. The signal detection efficiency can also be studied. With this we can further optimize our signal search and conduct background searches in a more rigorous way. Method III is the least explored and optimized in this work and thus could benefit most from future improvements. In method I there should be more study of the relative contribution of early and late echoes. We have reported that methods I and III have yet to find signals in events where method II produces relatively strong signals. This needs to be investigated further.

## V CONCLUSION

If compact binary mergers are forming horizonless exotic compact objects (ECOs) with reflecting interiors or boundaries then the resulting gravitational wave echoes can provide a striking confirmation.

By calculating the Green's function in the frequency space for ECOs with general potentials and boundary conditions, we found that the absolute value of the transfer function displays a resonance pattern as shown in Fig. 2. This pattern reveals some universal features, such as a nearly constant spacing resonance peaks, that we make use of here to search for echoes. This pattern also displays some non-universal features, such as an overall shift of the resonance peaks, that can be used in future studies to distinguish different ECO candidates.

Our search for echoes is based on the construction of window functions in both time and frequency. The primary feature of the window functions is a spacing determined by the time delay, while an optimization is performed with respect to the width, offset and the total number of the windows. The time and frequency windows are found to be complementary, with small and large numbers of echoes contributing respectively to a signal. By using correlation of two

windowed data sets, we have shown that the signal-to-noise ratio can be greatly enhanced and a good estimation for the true time delay can be obtained.

Applying these new search strategies to the LIGO data for the binary black holes mergers, we have explored a wider range of time delays than the previous template search. As shown in Fig. 7-10, tentative signals are found for multiple events, with an initial estimation of false-alarm probability of the signal(s) of any one event to be less than 1%. The best-fit time delays are consistent with new physics being characterized by the Planck length. We have not attempted to quantify the global significance of finding such signals in four of five events. We leave this for the reader to ponder, along with the dictum *extraordinary claims require extraordinary evidence*.

#### ACKNOWLEDGMENTS

We are grateful for useful discussions with participants of the conference "Quantum Black Holes in the Sky?" at Perimeter Institute, especially Jahed Abedi, Niayesh Afshordi, Ofek Bimholtz, Vitor Cardoso, Alex Nielsen, Julian Westerweck and Aaron Zimmerman. This research is supported in part by the Natural Sciences and Engineering Research Council of Canada. JR is supported in part by the Perimeter Institute for Theoretical Physics. Research at the Perimeter Institute is supported by the Government of Canada through the Department of Innovation, Science and Economic Development and by the Province of Ontario through the Ministry of Research and Innovation. This research has made use of data, software and/or web tools obtained from the LIGO Open Science Center (<https://losc.ligo.org>), a service of LIGO Laboratory, the LIGO Scientific Collaboration and the Virgo Collaboration. LIGO is funded by the U.S. National Science Foundation. Virgo is funded by the French Centre National de Recherche Scientifique (CNRS), the Italian Istituto Nazionale della Fisica Nucleare (INFN) and the Dutch Nikhef, with contributions by Polish and Hungarian institutes.

---

- [1] B. P. Abbott *et al.* [LIGO Scientific and Virgo Collaborations], Phys. Rev. Lett. **116**, no. 6, 061102 (2016) doi:10.1103/PhysRevLett.116.061102 [arXiv:1602.03837 [gr-qc]].
- [2] M. A. Abramowicz, W. Kluzniak and J. P. Lasota, Astron. Astrophys. **396**, L31 (2002) doi:10.1051/0004-6361:20021645 [astro-ph/0207270].
- [3] V. Cardoso and P. Pani, arXiv:1707.03021 [gr-qc]; Nat. Astron. **1**, 586 (2017) [arXiv:1709.01525 [gr-qc]].
- [4] B. Guo, S. Hampton and S. D. Mathur, arXiv:1711.01617 [hep-th].
- [5] V. Cardoso, E. Franzin and P. Pani, Phys. Rev. Lett. **116**, no. 17, 171101 (2016) Erratum: [Phys. Rev. Lett. **117**, no. 8, 089902 (2016)] [arXiv:1602.07309 [gr-qc]].

- [6] V. Cardoso, S. Hopper, C. F. B. Macedo, C. Palenzuela and P. Pani, Phys. Rev. D **94**, no. 8, 084031 (2016) [arXiv:1608.08637 [gr-qc]].
- [7] J. Abedi, H. Dykaar and N. Afshordi, Phys. Rev. D **96**, no. 8, 082004 (2017) [arXiv:1612.00266 [gr-qc]].
- [8] G. Ashton *et al.*, arXiv:1612.05625 [gr-qc].
- [9] C. Barcelo, R. Carballo-Rubio and L. J. Garay, JHEP **1705**, 054 (2017) [arXiv:1701.09156 [gr-qc]].
- [10] R. H. Price and G. Khanna, Class. Quant. Grav. **34**, no. 22, 225005 (2017) [arXiv:1702.04833 [gr-qc]].
- [11] H. Nakano, N. Sago, H. Tagoshi and T. Tanaka, arXiv:1704.07175 [gr-qc].
- [12] Z. Mark, A. Zimmerman, S. M. Du and Y. Chen, arXiv:1706.06155 [gr-qc].
- [13] A. Maselli, S. H. Vrba and K. D. Kokkotas, Phys. Rev. D **96**, no. 6, 064045 (2017) [arXiv:1708.02217 [gr-qc]].
- [14] J. Zhang and S. Y. Zhou, arXiv:1709.07503 [gr-qc].
- [15] P. Bueno, P. A. Cano, F. Goelen, T. Hertog and B. Vercnocke, arXiv:1711.00391 [gr-qc].
- [16] D. B. Sibandze, R. Goswami, S. D. Maharaj and P. K. S. Dunsby, arXiv:1702.04926 [gr-qc].
- [17] P. O. Mazur and E. Mottola, gr-qc/0109035.
- [18] M. Visser and D. L. Wiltshire, Class. Quant. Grav. **21**, 1135 (2004) [gr-qc/0310107].
- [19] B. Holdom and J. Ren, Phys. Rev. D **95**, no. 8, 084034 (2017) doi:10.1103/PhysRevD.95.084034 [arXiv:1612.04889 [gr-qc]].
- [20] V. Cardoso, L. C. B. Crispino, C. F. B. Macedo, H. Okawa and P. Pani, Phys. Rev. D **90**, no. 4, 044069 (2014) [arXiv:1406.5510 [gr-qc]].
- [21] M. Vallisneri *et al.* "The LIGO Open Science Center", proceedings of the 10th LISA Symposium, University of Florida, Gainesville, May 18-23, 2014; also arxiv:1410.4839.
- [22] B. P. Abbott *et al.* [LIGO Scientific and Virgo Collaborations], Phys. Rev. Lett. **116**, no. 24, 241103 (2016) doi:10.1103/PhysRevLett.116.241103 [arXiv:1606.04855 [gr-qc]].
- [23] B. P. Abbott *et al.* [LIGO Scientific and VIRGO Collaborations], Phys. Rev. Lett. **118**, no. 22, 221101 (2017) doi:10.1103/PhysRevLett.118.221101 [arXiv:1706.01812 [gr-qc]].
- [24] B. P. Abbott *et al.* [LIGO Scientific and Virgo Collaborations], Phys. Rev. Lett. **119**, no. 14, 141101 (2017) doi:10.1103/PhysRevLett.119.141101 [arXiv:1709.09660 [gr-qc]].
- [25] B. P. Abbott *et al.* [LIGO Scientific and Virgo Collaborations], arXiv:1711.05578 [astro-ph.HE].
- [26] E. Maggio, P. Pani and V. Ferrari, Phys. Rev. D **96**, no. 10, 104047 (2017) [arXiv:1703.03696 [gr-qc]].